

# WAVELET TRANSFORM SIGNAL PROCESSING TO DISTINGUISH DIFFERENT ACOUSTIC EMISSION SOURCES

K. S. DOWNS<sup>1</sup>, M. A. HAMSTAD<sup>2,3</sup> and A. O'GALLAGHER<sup>2</sup>

<sup>1</sup> Contractor to National Institute of Standards and Technology, Boulder, CO 80305-3328

<sup>2</sup> National Institute of Standards and Technology, Materials Reliability Division (853),  
325 Broadway, Boulder, CO 80305-3328

<sup>3</sup> Department of Engineering, University of Denver, Denver, CO 80208

## Abstract

A database of wideband acoustic emission (AE) modeled signals was used to continue to examine the use of wavelet-transform (WT) results to accomplish identification of AE sources. The AE signals in the database were created by use of a validated three-dimensional finite-element code. These signals represented the out-of-plane displacements from buried dipole sources in aluminum plates 4.7 mm thick with large lateral dimensions. The surface displacement signals at three distances (60, 120, and 180 mm) were filtered with a 40 kHz high-pass filter prior to applying the WT. The WTs were calculated with a freeware software program. The WT peak magnitudes were calculated at three key frequencies (i.e., 60, 270, and 522 kHz) for all the signals generated by three different source types (i.e., in-plane dipole, microcrack initiation, and balanced shear). The signal database covered seven different radiation angles (from 0° to 90°) and six or seven depths for each source type. The fundamental Lamb modes that corresponded to the WT peak magnitudes were also determined. It was concluded that the variation of the normalized peak WT magnitudes as a function of the radiation angles was effectively constant for the various source depths. This effective independence of source depth was demonstrated for a fixed source type, propagation distance, and key frequency-mode combination. The fact that the radiation-angle dependence varied among source types for particular frequency-mode combinations allowed ratios of the WT peak magnitudes at different radiation angles to be used to uniquely distinguish the different source types.

**Keywords:** Acoustic emission; Acoustic emission modeling; AE; Finite-element modeling; Source identification; Wavelet transform; Wideband acoustic emission.

Contribution of the U.S. National Institute of Standards and Technology; Not subject to copyright in the United States. Trade names in this paper are included for information only; endorsement is neither intended nor implied.

## 1. Introduction

A previous attempt by two of the authors to use results from a wavelet transform (WT) to distinguish different acoustic emission (AE) sources types was not fully successful [1]. The previous effort examined only two frequency-mode combinations, namely the fundamental anti-symmetric mode ( $A_0$ ) at 50 kHz and the fundamental symmetric mode ( $S_0$ ) at 522 kHz. A ratio of the peak WT magnitude of the  $A_0$  mode at 50 kHz to the peak WT magnitude of the  $S_0$  mode at 522 kHz successfully distinguished different source types based on far-field AE signals originating from sources at the same depth, for AE signals propagating only in the 0°, x-axis direction. (Note: throughout this paper, the term "far-field" implies that the Lamb modes have developed in the recorded AE signals.) However, when the depth of the AE sources below the plate

surface was changed, the technique was no longer successful. Specifically, the mixed-mode  $A_0/S_0$  ratios of the WT magnitudes changed as the source depth changed, thus resulting in ratio values that overlapped for the different source types [1].

In this current research, it was also found that the inclusion of data from multiple radiation angles did not eliminate the problems encountered when using the mixed-mode  $A_0/S_0$  ratio approach to determine source types for multiple different source depths. Thus, it was desired to create a different analytical approach for source type identification free from the effects of variations in source depths.

It was noted that Buttle and Scruby [2, 3] successfully identified different sources with a radiation-pattern approach in the near field, and the present authors observed that the different AE source types studied here have different radiation patterns [4, 5]. Thus the present authors used these radiation patterns successfully to develop a single-mode WT ratio technique (incorporating ratios of WTs for a single mode at various radiation angles) to distinguish different AE source types from far-field AE signals (even having various source depths) when the source location is already known.

Some key differences in the present work versus the authors' previous effort are as follows: (a) the present effort used data from multiple radiation directions for a given AE event, whereas the prior work used only data from the 0 degree propagation direction; (b) the present effort examined data and associated ratios of WT magnitudes for only a single mode at a time (either the  $A_0$  or  $S_0$ ) for two different angles, versus the approach in the prior effort using a mixed-mode  $A_0/S_0$  ratio for a single angle; and, (c) the present effort examined six frequency-mode combinations (i.e.,  $A_0$  at 60 kHz;  $A_0$  at 270 kHz;  $A_0$  at 522 kHz;  $S_0$  at 60 kHz;  $S_0$  at 270 kHz; and  $S_0$  at 522 kHz) versus only two combinations in the prior effort.

The AE source-identification approach that was successfully developed used AE signals in the far-field, which were generated by finite-element modeling (FEM) in a plate of large lateral dimensions. Since the FEM technique created a definitive knowledge of the modeled AE sources, the signal processing results could be related to the different source types in an unambiguous fashion.

To the authors' knowledge, no other comprehensive study has been published where the results of forward modeling have been used to develop and validate an AE source identification methodology for far-field signals. Work published by Buttle and Scruby [2, 3] used forward modeling to develop signal-processing techniques to distinguish source types in the near-field. In their case, the AE signals (bulk waves) were obtained from the direct path to the sensors located at different radiation angles. Their approach is in contrast to the work reported here in which the AE signals propagate into the far-field so that the various Lamb modes are present.

## **2. Brief Description of the FEM-based AE Signal Database**

A detailed description of the development of an extensive AE signal database was given previously [1]; a subset of this database was used in the present effort. Hence, only certain key or additional aspects are highlighted here. The FEM signals were generated in an aluminum plate (1 m x 1 m x 4.7 mm). The signals represent the out-of-plane top surface displacement as recorded by a flat-with-frequency point-contact sensor. Each FEM signal calculation started at the beginning of the operation of the source (rise time of 1.5  $\mu$ s) and continued for 200  $\mu$ s; the

displacement signals were calculated at time increments of 44.6 ns. Due to the lateral size of the plate, plate-edge reflections did not superimpose on the direct arrival of the signals. More specifically, the edge-reflected signals typically appear from about 150  $\mu\text{s}$  to the calculation end (at 200  $\mu\text{s}$ ) for signals with a propagation distance of 180 mm. At shorter propagation distances, the edge reflections occur at later times. The AE signals were modeled for three in-plane propagation distances (60 mm, 120 mm, 180 mm) and seven in-plane radiation angles ( $0^\circ$ ,  $12^\circ$ ,  $22.5^\circ$ ,  $45^\circ$ ,  $67.5^\circ$ ,  $78^\circ$ , and  $90^\circ$ ). Also, a total of three AE source types composed the database subset used here: (a) a single in-plane dipole in  $0^\circ$  direction (x-axis); (b) a microcrack initiation with major axis in  $0^\circ$  direction (x-axis); and, (c) a shear about the y-axis with the shear directions at  $45^\circ$  to the x-axis with no net moment. The depths from the top of the plate surface of the modeled sources were 2.35, 2.037, 1.723, 1.41, 1.097, and 0.783 mm for all three source types. Additionally, the in-plane dipole had one more source depth of 0.47 mm.

Figure 1 shows the three source types and their orientation relative to the x-y-z plate coordinate system. This figure also shows reference  $0^\circ$  and  $90^\circ$  directions used for the seven radiation directions. The assumption of the relevance of these sources to real AE experiments is based on assuming the real plate is being stressed in the x-direction. Thus, the dominant dipole for the microcrack initiation is oriented in that direction. Also, the shear (without a resultant moment) at  $45^\circ$  about the y-axis represents the case of a dislocation type source on the planes of maximum shear for axial loading. Finally, the in-plane dipole in the x-direction could approximately represent the fracture of a fiber aligned in that direction for an aluminum metal-matrix composite with a low fiber volume. All the dipoles had 1 N force except for the microcrack initiation source dipoles in the y and z directions, where the forces were 0.52 N. The centers of the sources were located at six or seven depths (z-axis) below the top surface of the plate. Only six depths are available in some cases, since the authors have determined that locating one of the monopoles (which make up the dipoles) as a body force in a FEM cell adjacent to the plate surface alters the results in a small but observable way. The authors believe this effect is due to a “mixing” of the plate surface boundary conditions as a result of the structure of the finite-element program. In essence, the body force interferes with the assumption of a stress-free plate surface at this cell for the intended internal dipole.

### 3. Description of Signal Processing and Feature Extraction

All the FEM-calculated AE signals were processed in the following fashion. Prior to performing the WT, the FEM-calculated signals were all numerically filtered with a 40 kHz four-pole Butterworth high-pass filter. Then the signals were re-sampled from their original time increment of 44.6 ns to a time increment of 0.1  $\mu\text{s}$ , and the signal was extended with zeroes beyond 200  $\mu\text{s}$ , for a total of 8192 points in each signal.

Each adjusted FEM signal had a wavelet transform performed upon it using a software program called AGU-Vallen Wavelet version R2002.0703 [6]. For each WT computation, a number of processing parameters must be specified. The following Wavelet Transformation Settings were used: maximum frequency = 700 kHz; frequency resolution = 3 kHz; wavelet size = 600 samples. The following Wavelet Time Range Settings were used: number of samples (i.e., points) = 800 for 60 mm distances, 1200 for 120 mm distances, and 1500 for 180 mm distances; offset samples = 0. By this choice of number of samples, all edge reflections were eliminated from consideration.

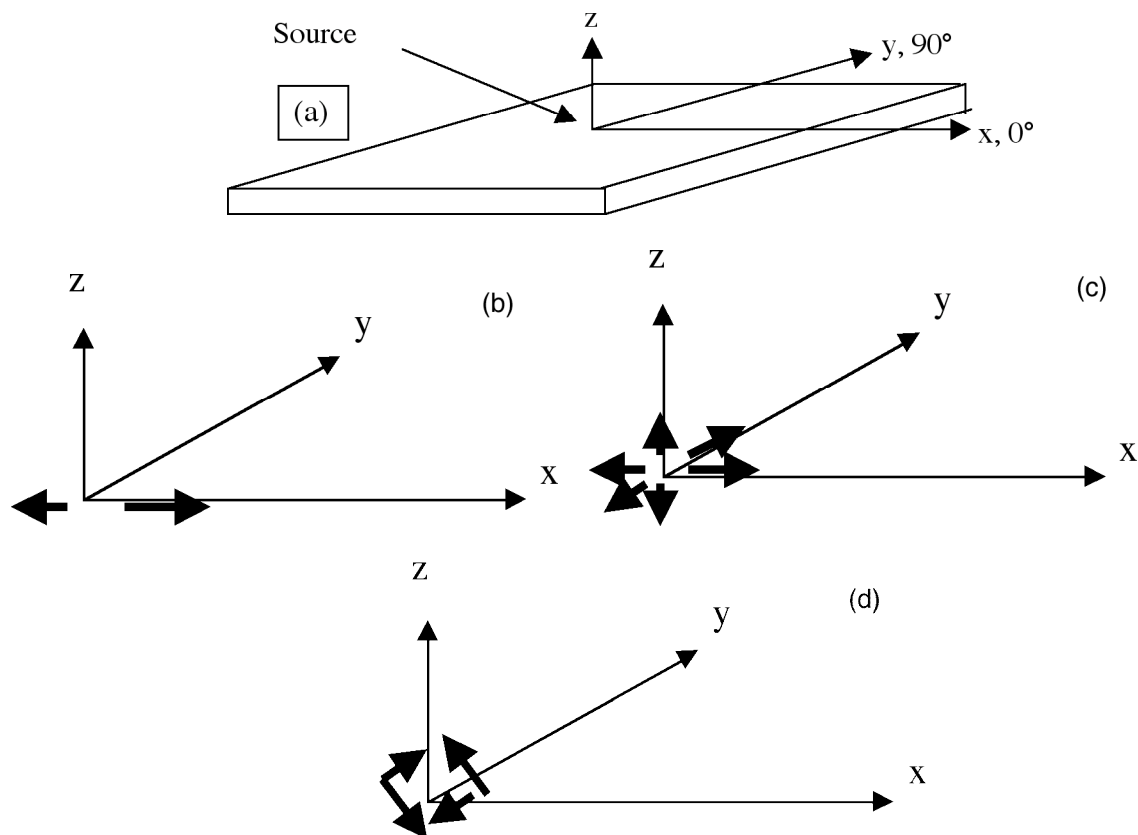


Fig. 1 Coordinate systems: (a) used with source propagation plate and radiation angles; (b) in-plane dipole source; (c) microcrack initiation source; (d) balanced shear (zero moment)  $45^\circ$  about y-axis.

The resulting output for each wavelet transform consists of numerical values for the WT magnitude as a function of both time and frequency. This output can be viewed numerically in a spreadsheet format, or in a more qualitative, graphic format where various colors are used to indicate the WT magnitude on a time-vs.-frequency plot. A software feature also allows superposition of the Lamb-wave group velocities onto the graphical WT result; however, knowledge of the propagation distance is required to correctly superimpose the group velocity curves. See WT examples (with superimposed group-velocity curves) and further processing details in references [7] and [8; Fig. 2].

For each WT, several features were extracted and recorded. First, the absolute maximum WT magnitude for the entire time-frequency continuum examined was noted. Next, the predominant mode ( $A_0$  or  $S_0$ ) was determined and recorded at the 60 kHz frequency using the superimposed group-velocity curves. Additionally, the peak WT magnitude at 60 kHz was recorded. The process was repeated, and similar peak WT magnitudes and their associated modes were recorded for the 270 and 522 kHz frequencies for each WT. These features as extracted at the three key frequencies were studied extensively as described later in this paper.

#### 4. Terminology and Related Discussion

To discuss the background research and the new approach presented here for source type identification, it is necessary to introduce some concepts and terminology detailed in a related companion paper on WT-based source location [8]. In that related research, a much larger data

base of AE signals was used encompassing eight various dipole-based AE sources at various source depths and radiation angles in a 4.7 mm thick aluminum plate. The three source types that were examined in the effort described in this paper are a subset of this larger database. After manually examining WTs for the entire, larger database of eight source types, it was determined that three “key” frequencies and their associated modes at those frequencies could characterize all the potentially most energetic regions that could appear in the WTs of the larger database. It would be most accurate to further explain that each of the key frequencies is actually a band 3 kHz wide across which the WT magnitude was effectively averaged by the 3 kHz resolution chosen for the WT computation. These three “key” frequencies were 60 kHz, 270 kHz, and 522 kHz. A more detailed discussion of the process used to identify these three key frequencies can be found in reference [8].

As noted earlier, the peak WT magnitude was determined at each of the three key frequencies for each AE signal. For each WT examined, each of the three frequencies of interest was given one of three labels based on their peak WT magnitudes. The frequency having the greatest peak WT magnitude as a function of time was defined as the “primary” frequency for that particular WT; in a similar fashion, the other two frequencies examined were ranked with respect to their peak WT magnitudes (in descending order) as “secondary” and “tertiary.” The frequency-labeling process was repeated for each WT.

Several noteworthy observations were made when the frequency-labeling results of the WTs for the FEM AE signals were examined and combined with the already recorded modes and WT magnitudes for the key frequencies. The peak WT magnitude for the primary frequency was typically quite close in value to the absolute maximum WT magnitude for the entire signal examined, and the theoretical arrival time for its associated portion of the fundamental Lamb mode ( $A_0$  or  $S_0$ ) corresponded closely to the arrival time of the peak WT magnitude for that frequency. It was further observed that when a primary frequency occurred at 60 kHz, the mode that corresponded to the arrival time of the peak WT magnitude was always  $A_0$ , whereas when the primary frequency occurred at 270 kHz or 522 kHz, its actual mode was always  $S_0$ . Thus, the term “principal mode” was defined as the  $A_0$  mode for 60 kHz, and as the  $S_0$  mode for 270 and 522 kHz. In summary, each primary frequency WT peak magnitude always represented the principal mode for that frequency, whereas the WT peak magnitudes of secondary and tertiary frequencies may have represented either the principal mode or an alternate mode for that frequency.

Additionally, for secondary or tertiary frequencies, the plot of WT magnitude versus time could be used to determine the arrival time of a particular fundamental mode at the frequency of interest even if a non-principal (i.e., alternate) mode were present. The ability to determine the arrival times of modes other than that of the WT peak at a certain frequency was also enhanced by the knowledge of the signal propagation distance and the known theoretical group velocity curves.

For a given source type and as a function of source depth, certain frequencies no longer appeared as the primary frequency. In fact, the WT magnitude of the mode at these frequencies can become quite small. For example, when source depths were very near the plate surface, the WT for the  $S_0$  mode peak at 522 kHz no longer had significant magnitude. In a similar fashion, when source depths were quite near the mid-plane of the plate, the WT for the  $A_0$  mode peak at 60 kHz no longer had significant magnitude.

## 5. Single-Mode WT Ratio Approach for Source Identification

Based upon these concepts and the terminology described above, the authors propose an alternate source identification methodology based on single-mode WT ratios as follows. Each combination of a given source type and source depth was considered separately. Specifically, each of the peak WT magnitudes (at the three frequencies of interest, i.e., 60 kHz, 270 kHz, and 522 kHz), for all the radiation angles was normalized using the zero-degree peak WT magnitude at that source depth and frequency, as long as the zero-degree data had the same mode as for the angle being normalized. In a few cases, the peak mode at a given frequency for various non-zero radiation angles differed from the zero-degree peak mode; in those cases, the non-zero degree data were normalized using a lower magnitude WT peak from the zero-degree data for the proper mode. In other words, two different modes (i.e., both  $A_0$  and  $S_0$  modes) were occasionally present in a signal (for a given source type and depth) at the frequency of interest; sometimes the relative magnitudes of these two peaks gradually shifted as the radiation angle changed. The peak WT magnitude of the  $A_0$  mode at  $0^\circ$  was used to normalize the data from other radiation angles where the  $A_0$  mode predominated; similarly the peak WT magnitude of the  $S_0$  mode at  $0^\circ$  was used to normalize the data from other radiation angles where the  $S_0$  mode predominated. In a few cases, the predominant mode at a non-zero radiation angle was of a mode that had no localized peak WT magnitude for the  $0^\circ$ -angle data; thus, no normalized WT value could be computed for that particular non-zero radiation angle.

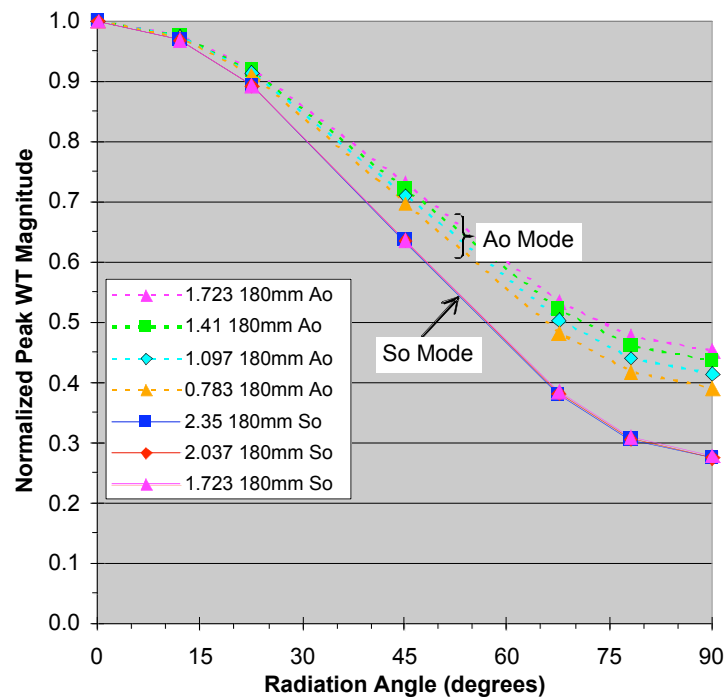


Fig. 2 Normalized peak WT magnitudes for microcrack source at 270 kHz; legend lists source depth (mm), propagation distance (mm), and mode.

Figure 2 plots normalized WT magnitude values versus radiation angle for a series of source depths for a microcrack source, frequency: 270 kHz, propagation distance: 180 mm; the figure includes both  $A_0$  and  $S_0$  modes. While this plot displays data for only a single combination of source type, frequency, and propagation distance, it is representative of many trends that were observed for all the data. First,  $A_0$  data are often (although not always) significantly different from  $S_0$  data; thus it was decided to treat and consider results from each mode separately in all

Table 1 Source depths of the normalized peak WT magnitudes that were averaged for  $A_0$  mode for each combination of frequency, source type, and radiation angle.

Frequency (kHz)	Source Type	Radiation Angles ( $^\circ$ )	Depths for which normalized peak WT magnitudes were averaged for each angle shown	
			Propagation Distance	
			60 mm	180 mm
60	In-plane dipole	0, 12, 22.5, 45, 67.5, 78	2.037, 1.723, 1.41, 1.097, 0.783, 0.47	2.037, 1.723, 1.41, 1.097, 0.783, 0.47
		90	none	2.037, 1.723, 1.41, 1.097, 0.783, 0.47
	Micro-crack	0, 12, 22.5, 45, 67.5, 78, 90	2.037, 1.723, 1.41, 1.097, 0.783	2.037, 1.723, 1.41, 1.097, 0.783
	Shear	0, 12, 22.5, 45, 67.5, 78, 90	2.037, 1.723, 1.41, 1.097, 0.783	2.037, 1.723, 1.41, 1.097, 0.783
270	In-plane dipole	0, 12, 22.5, 45, 67.5	1.41, 1.097, 0.783, 0.47	1.41, 1.097, 0.783, 0.47
		78	1.097, 0.783, 0.47	1.41, 1.097, 0.783, 0.47
		90	0.783, 0.47	1.41*, 1.097*, 0.783, 0.47
	Micro-crack	0, 12, 22.5	1.41, 1.097, 0.783	1.723*, 1.41, 1.097, 0.783
		45, 67.5, 78, 90	1.41, 1.097, 0.783	1.723, 1.41, 1.097, 0.783
	Shear	0, 12, 22.5, 45	1.097, 0.783	1.41*, 1.097, 0.783
67.5, 78, 90		1.097, 0.783	1.097, 0.783	
522	In-plane dipole	0, 12, 22.5, 45, 67.5, 78	0.47	0.47
		90	0.47*	0.47*
	Micro-crack	0, 12, 22.5, 45, 67.5, 78, 90	none	0.783
	Shear	0, 12, 22.5, 45, 67.5, 78, 90	none	none

\* Indicates that the WT magnitude for this depth (for the angles indicated) was normalized by a *localized* peak WT magnitude of the proper mode for  $0^\circ$  radiation angle data, (since the *maximum* WT peak at  $0^\circ$  had a different mode)

further analysis. Next, it is clear that the normalization does in fact eliminate significant effects due to source depths, as long as data results are considered for any one source type, one frequency, one particular mode ( $A_0$  or  $S_0$ ), and one propagation distance. Although each of the six different source depths for each mode is represented by a separate line on Fig. 2, the lines overlap so much for the  $S_0$  mode that many of the lines cannot be seen individually. Because of the great similarity in results across the depths, it was decided to average the information for all source depths that overlapped or nearly overlapped for each combination of source type, frequency, propagation distance, and radiation angle. It is important to note that for each possible combination, the information for  $A_0$  modes was averaged separately from the information for  $S_0$  modes. Since a given depth for a given signal case and frequency usually represented either the  $A_0$  or  $S_0$  mode (but not both), only certain depths were averaged for each mode. Also, if the results at a certain depth did not sufficiently overlap, that depth was not included in the average.

Tables 1 and 2 summarize which depths were averaged for each mode, radiation angle, frequency, source type, and propagation distance.

Table 2 Source depths of the normalized peak WT magnitudes that were averaged for S<sub>0</sub> mode for each combination of frequency, source type, and radiation angle.

Frequency (kHz)	Source Type	Radiation Angles (°)	Depths for which normalized peak WT magnitudes were averaged for each angle shown	
			Propagation Distance	
			60 mm	180 mm
60	In-plane dipole	0, 12, 22.5, 45	2.35	2.35
		67.5, 78, 90	none	none
	Micro-crack	0, 12, 22.5, 45, 67.5, 78, 90	2.35	2.35
	Shear	0, 12, 22.5, 45, 67.5, 78, 90	2.35	2.35
270	In-plane dipole	0, 12, 22.5, 45, 67.5, 78	2.35, 2.037, 1.723	2.35, 2.037, 1.723, 1.41*, 1.097*
		90	2.35, 2.037, 1.723	2.35, 2.037, 1.723, 1.41, 1.097
	Micro-crack	0, 12, 22.5	2.35, 2.037, 1.723	2.35, 2.037, 1.723
		45	2.35, 2.037, 1.723*	2.35, 2.037, 1.723*
		67.5, 78, 90	2.35, 2.037	2.35, 2.037, 1.723*
	Shear	0, 12, 22.5, 45	2.35, 2.037, 1.723, 1.41	2.35, 2.037, 1.723, 1.41
		67.5, 78, 90	2.35, 2.037, 1.723	2.35, 2.037, 1.723, 1.41
	522	In-plane dipole	0, 12, 22.5, 67.5, 78	2.35, 2.037, 1.723, 1.41, 1.097, 0.783
45, 90			2.35, 2.037, 1.723, 1.41, 1.097, 0.783	2.35, 2.037, 1.723, 1.41, 1.097, 0.783*
Micro-crack		0, 12, 22.5	2.35, 2.037, 1.723, 1.41, 1.097	2.35, 2.037, 1.723, 1.41, 1.097
		45	2.35, 2.037, 1.723, 1.41	2.35, 2.037, 1.723, 1.41
		67.5	2.35, 2.037, 1.723	2.35, 2.037, 1.723*
		78, 90	none	none
Shear		0, 12, 22.5, 45	2.35, 2.037, 1.723, 1.41, 1.097, 0.783	2.35, 2.037, 1.723, 1.41, 1.097, 0.783
		67.5, 78, 90	2.35, 2.037, 1.723, 1.41, 1.097	2.35, 2.037, 1.723, 1.41, 1.097

\* Indicates that the WT magnitude for this depth (for the angles indicated) was normalized by a *localized* peak WT magnitude of the proper mode for 0° radiation angle data, (since the *maximum* WT peak at 0° had a different mode)

Figure 3 shows a plot of averaged normalized values of peak WT magnitudes as a function of radiation angle for an in-plane dipole source; separate curves are shown for propagation distances of 60 mm and 180 mm. It should be noted here that the data for all three propagation distances (60, 120, and 180 mm) were initially examined in a preliminary fashion. For efficiency purposes only, it was then decided to focus upon the two extreme distances, namely 60 and 180 mm. Figures 4 and 5 show similar results for a microcrack and balanced shear source, respec-

tively. The main point to be gained from these figures is that the curves for propagation distances of 60 mm and 180 mm are very similar to each other, and often times are directly overlapping.

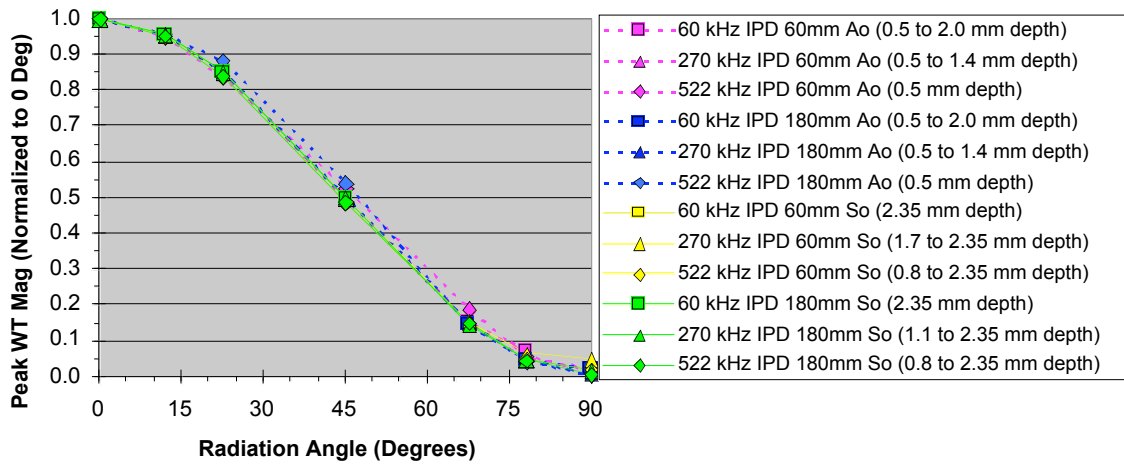


Fig. 3 Averaged results for 60 mm versus 180 mm propagation distance for in-plane dipole source.

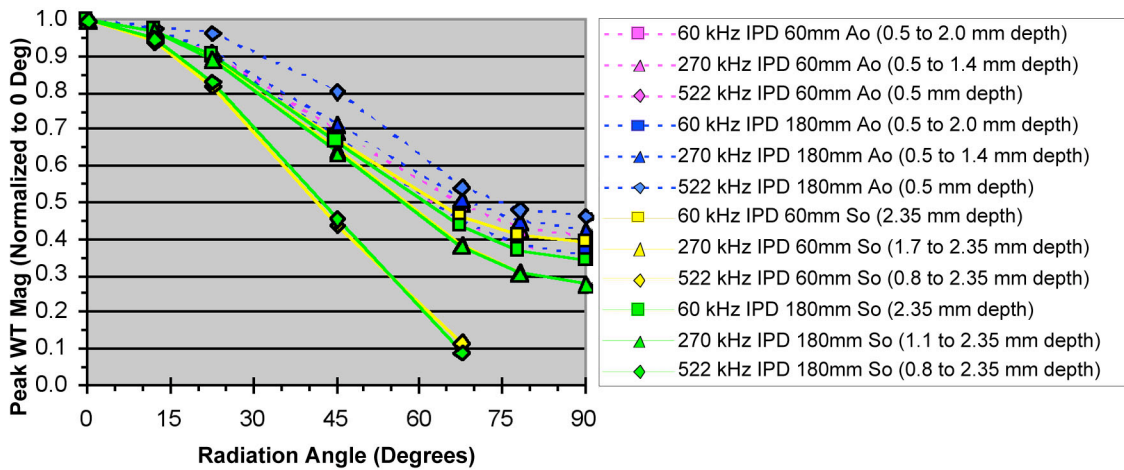


Fig. 4 Averaged results for 60 mm versus 180 mm propagation distance for microcrack initiation source.

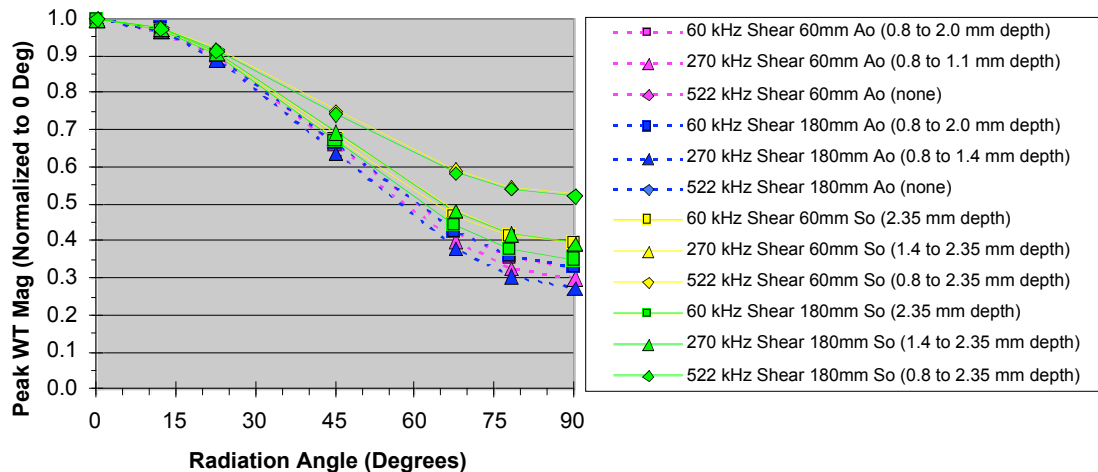


Fig. 5 Averaged results for 60 mm vs. 180 mm propagation distance for balanced shear source.

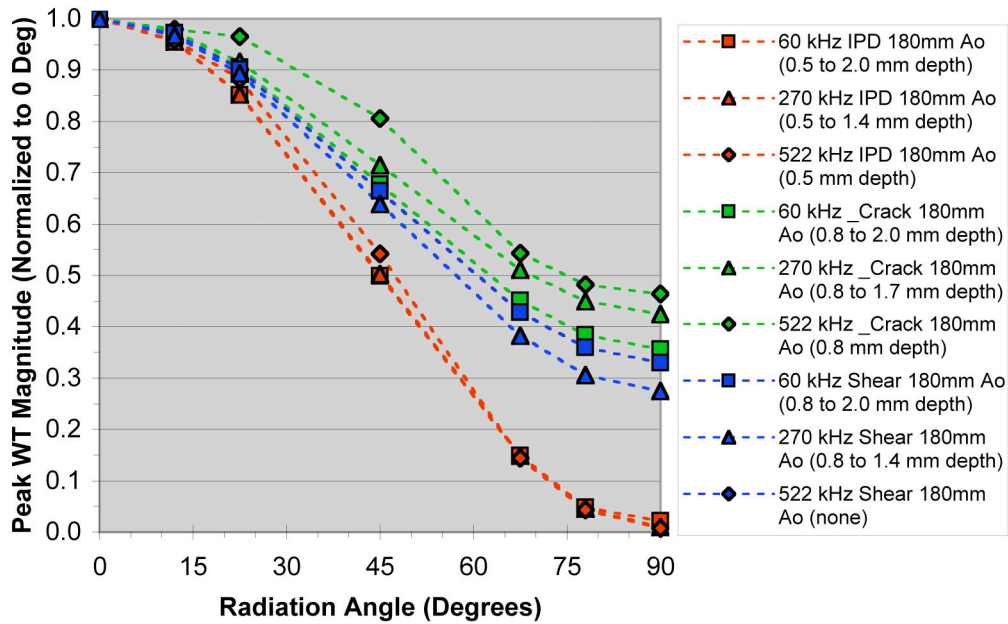


Fig. 6 Normalized peak WT magnitudes for  $A_0$  mode (averaged for multiple depths) for all three source types for 180 mm propagation distance.

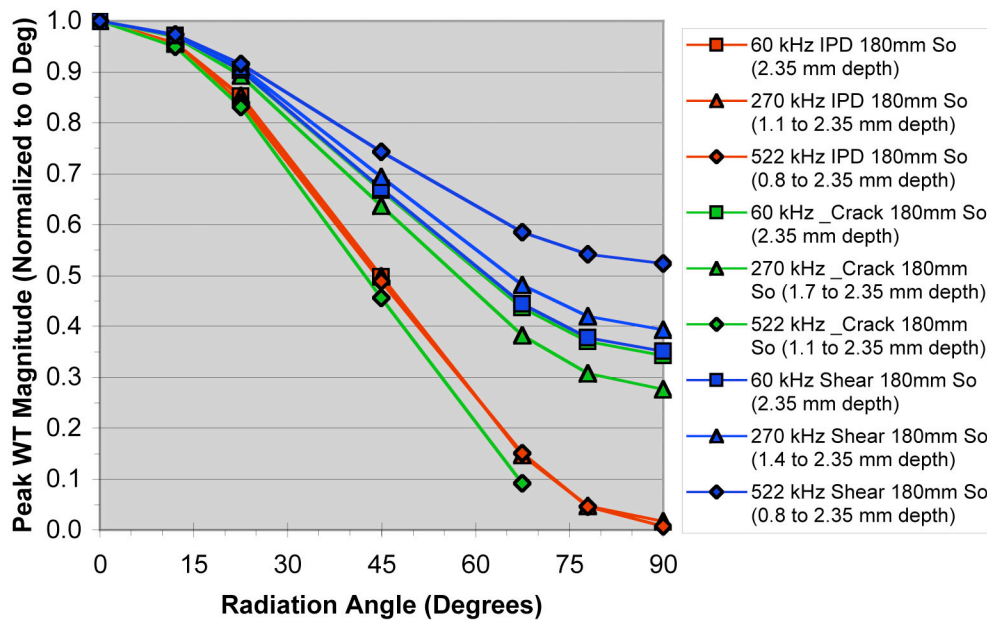


Fig. 7 Normalized peak WT magnitudes for  $S_0$  mode (averaged for multiple depths) for all three source types for 180 mm propagation distance.

Because of the great similarity in the normalized results for all three source types for the two extreme propagation distances of 60 and 180 mm, all further analysis in this paper focused upon data from only the 180 mm propagation distance. Discussion later in this paper examines in more detail the effects of different propagation distances on WTs. It is worth briefly noting here that in some cases there are two different modes that have nearly the same arrival time in the 60 mm data; however, in the 180 mm data, the dispersion effects of the signals over the greater

propagation distance result in a separation in arrival times of the two modes, thus making the 180 mm data more useful for the development and application of a source-identification scheme.

Figures 6 and 7 show plots for all three source-types of the averaged normalized peak WT magnitudes versus radiation angle for the  $A_0$  and  $S_0$  modes, respectively. For these plots, the curves have been color coded as follows: red indicates an in-plane dipole source; green indicates a microcrack initiation source; and, blue indicates a balanced-shear source. One can readily see in both Figs. 6 and 7 that for certain curves the different source types are distinct, and the differences in normalized peak WT magnitudes generally become greater as the radiation angle increases (with almost no difference in normalized peak WT values at very small angles); such trends imply that one can uniquely distinguish source types for an event of unknown source. Because the curves in Figs. 6 and 7 are not linear, it was hoped that further data manipulation could enhance the source differences already evident in Figs. 6 and 7. Thus, a set of 21 ratios was created for each curve (i.e., for each combination of a given frequency, source type, and mode) shown on Figs. 6 and 7. The ratios were created by comparing normalized WT magnitude data for one radiation angle to another radiation angle for the same curve. For example, the ratios compared data for  $90^\circ$  to  $78^\circ$ ;  $90^\circ$  to  $67.5^\circ$ ;  $90^\circ$  to  $45^\circ$ ;  $90^\circ$  to  $22.5^\circ$ ;  $90^\circ$  to  $12^\circ$ ;  $90^\circ$  to  $0^\circ$ ;  $78^\circ$  to  $67.5^\circ$ ; etc., for all 21 possible ratio combinations for the seven different radiation angles.

Figures 8 through 11 summarize four examples of these ratio results, which use the same red-green-blue color coding for the three source types. These four examples were chosen because they are the frequency-mode combinations that occur most often in the frequency-based WT peak magnitudes for the whole database. The authors note that the  $S_0$  mode results pertain most often to source depths nearer the plate midplane, and the  $A_0$  mode results pertain most often to source depths nearer the plate surfaces. Also, in Fig. 9 there are no ratios shown that include data for the angles of  $78^\circ$  or  $90^\circ$  for the microcrack source having  $S_0$  mode at 522 kHz because the signal had insufficient energy to define a correct mode arrival time.

Ideally one would wish to identify a ratio in which all three source types have a significant normalized peak WT magnitude (to allow for concerns presented by the presence of electronic noise in empirically recorded AE signals), yet in which there are also the greatest differences among the three source types. It is worth noting that, for all four examples examined, the greatest distinctions among source types are apparent for ratios including greater radiation angles, and the ratios using only smaller angles show almost no distinction between source types. From this observation, one might be tempted to rely heavily on the data from these greater radiation angles to identify source types. However, a discussion of peak WT magnitudes is first warranted.

Figures 12-14 show the absolute peak WT magnitudes (without regard to frequency) for the various source types and source depths as a function of radiation angle. An examination of the underlying data shows that as the source depth increases toward the mid-plane, the significant amplitude of the antisymmetric mode decreases and the symmetric mode amplitude increases (albeit at a rate slower than that at which the antisymmetric mode amplitude changes). A minor exception to this trend occurs for the in-plane dipole and microcrack sources, which show a slight increase in the symmetric-mode amplitude near the plate surface; this exception might be accounted for due to reduced constraint because of the presence of a nearby free surface. The net overall effect of the antisymmetric-mode and symmetric-mode trends is that the greatest peak WT magnitudes occur for AE sources near the plate surface for all three source types, with decreasing peak WT magnitudes at greater source depths.

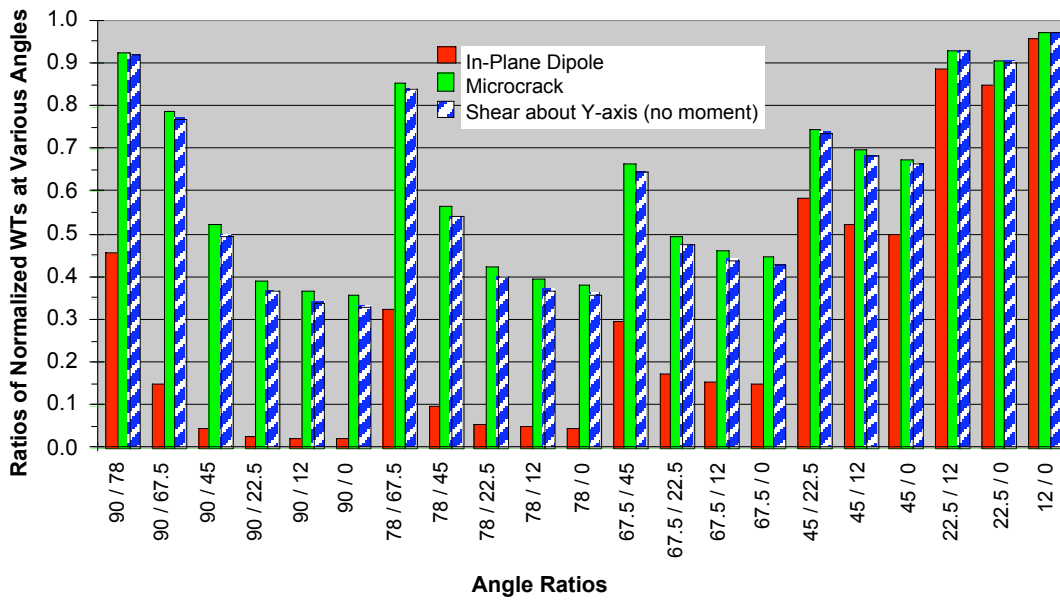


Fig. 8 Ratios of normalized peak WT magnitudes for A<sub>0</sub> mode at 60 kHz at various radiation angles for all three source types.

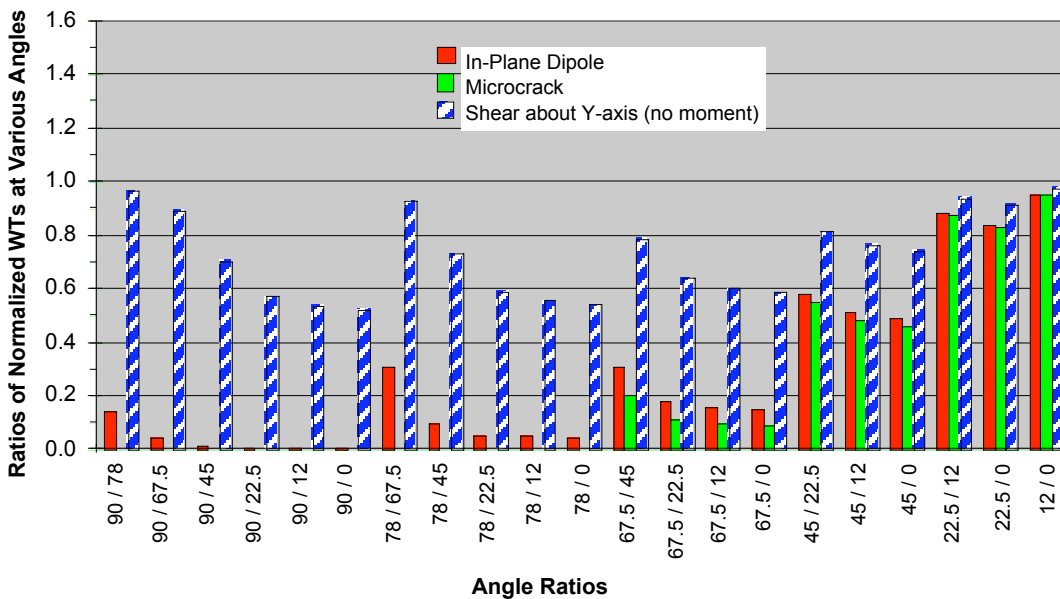


Fig. 9 Ratios of normalized peak WT magnitudes for S<sub>0</sub> mode at 522 kHz at various radiation angles for all three source types.

More importantly, one should note that the absolute peak magnitudes of the WT signals fall off (sometimes dramatically) at greater radiation angles. For all three source types, the rate at which the WT signal falls off is most dramatic for sources nearest the plate surface. Of the WT magnitudes for the three source types, the in-plane dipole falls off most dramatically overall (with its 90° magnitude generally being only about 2% of its original 0° degree magnitude); microcrack WT magnitudes are the least for the three source types at 0°, but they fall off much more moderately (with their 90° magnitude being about one-third of their original 0° magnitude); the shear source has the greatest 0° WT magnitudes of the three source types, and also falls off moderately (with its 90° magnitude being about one-third to one-half of its 0° magnitude).

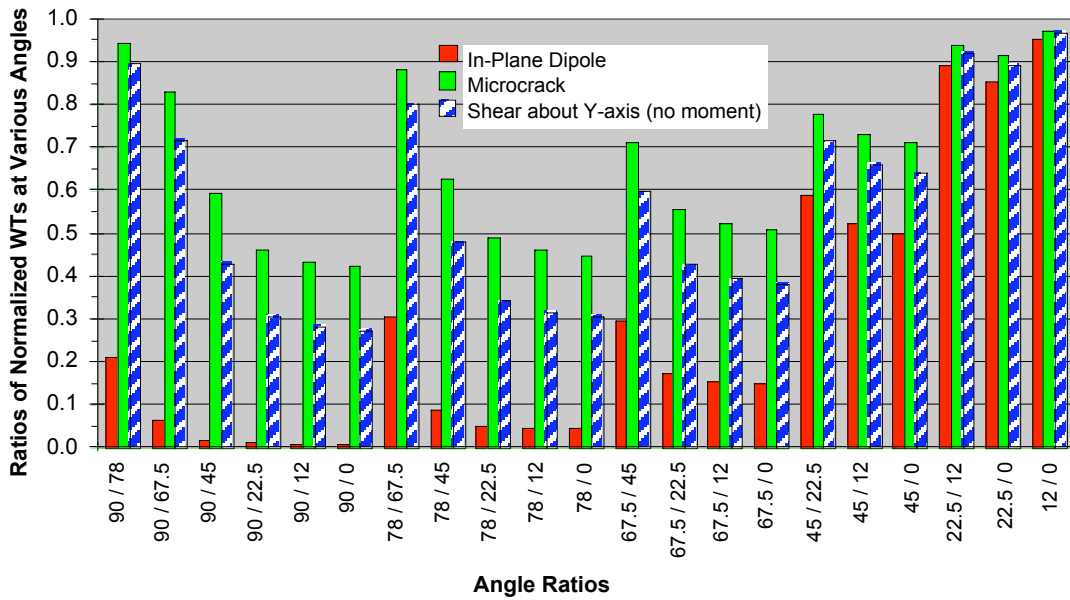


Fig. 10 Ratios of normalized peak WT magnitudes for  $A_0$  mode at 270 kHz at various radiation angles for all three source types.

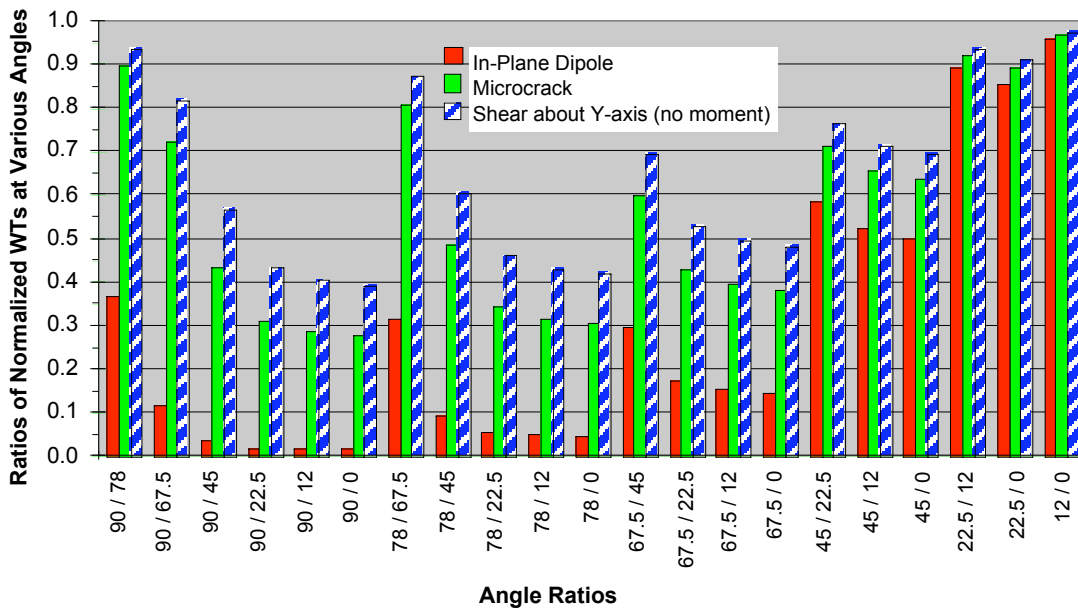


Fig. 11 Ratios of normalized peak WT magnitudes for  $S_0$  mode at 270 kHz at various radiation angles for all three source types.

Thus, the data curves and ratios (in Figs. 6 through 14) show two opposing trends: the greatest distinctions between source types are at the greatest radiation angles, but these greater radiation angles have peak WT magnitudes that have fallen off significantly from the original  $0^\circ$  values, and perhaps are so small as to be not usable, particularly for some sources near the mid-plane of the plate. If one wishes to choose the most appropriate ratio to use in distinguishing the three source types from each other, one must therefore make a compromise choice that leans toward using data from moderate radiation angles (perhaps  $22^\circ$  to  $67.5^\circ$  or so in the numerator, and  $0^\circ$  to  $45^\circ$  or so in the denominator) to ensure that the signal magnitude and source-type distinctions are both sufficient.

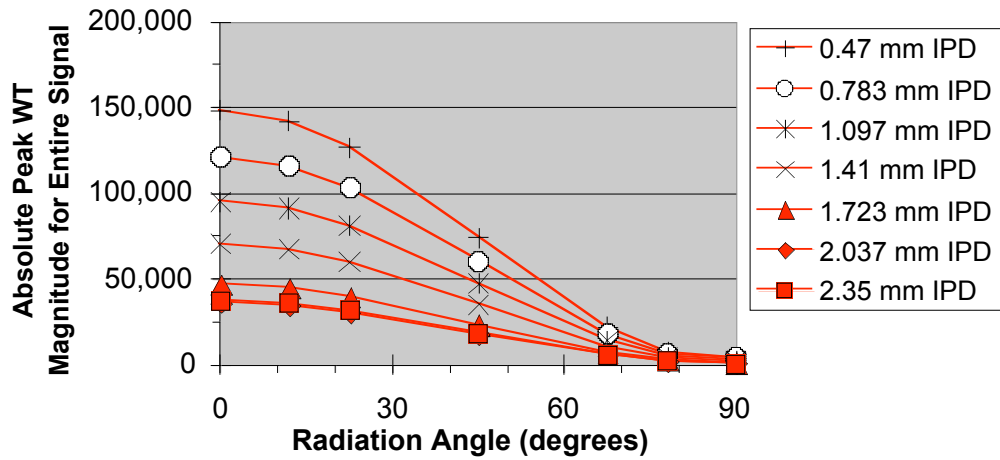


Fig. 12 Absolute peak WT magnitudes vs. radiation angle for various source depths for in-plane dipole source at 180 mm propagation distance.

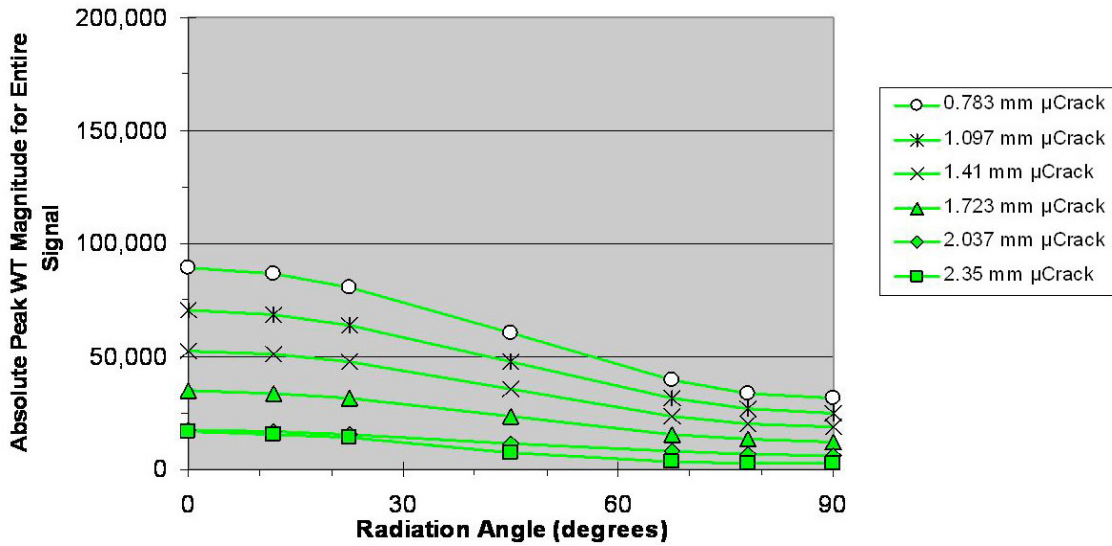


Fig. 13 Absolute peak WT magnitudes vs. radiation angle for various source depths for microcrack initiation source at 180 mm propagation distance.

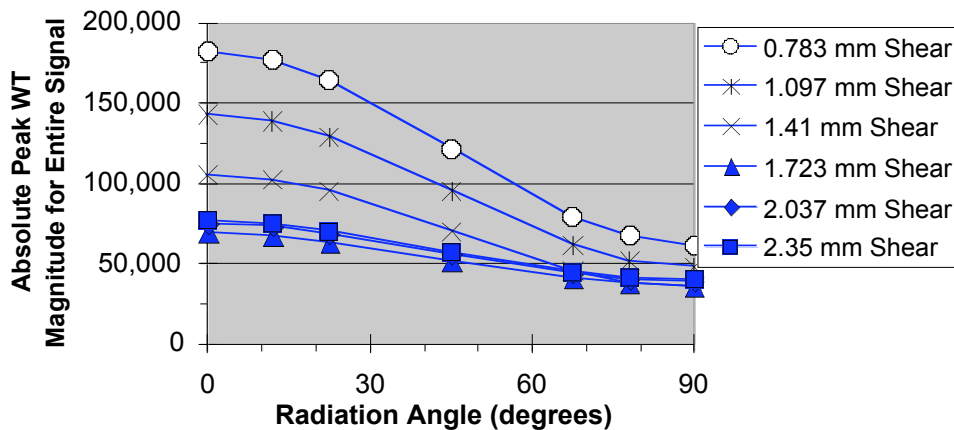


Fig. 14 Absolute peak WT magnitudes vs. radiation angle for various source depths for balanced shear source at 180 mm propagation distance.

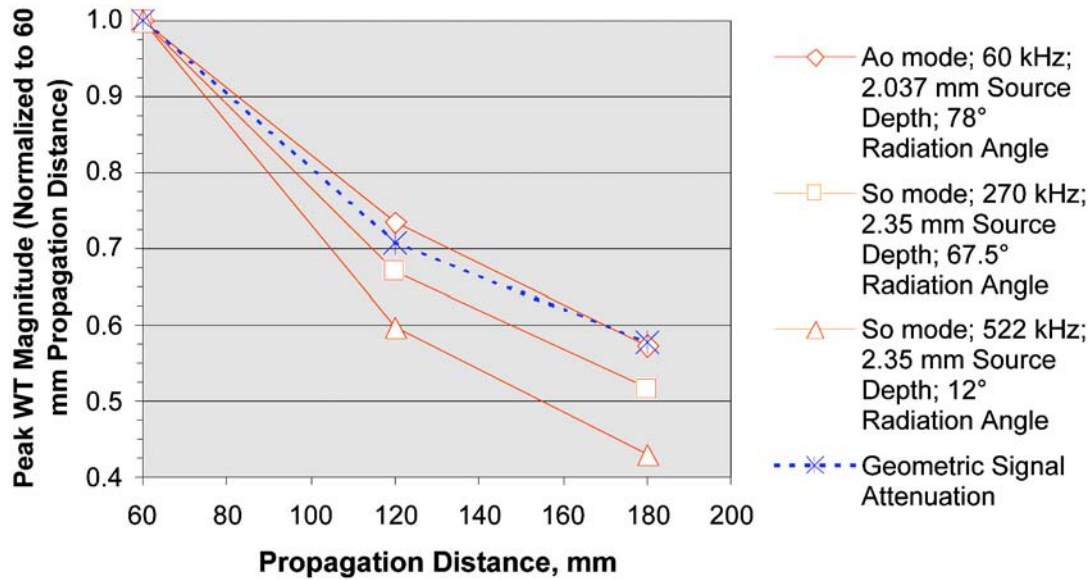


Fig. 15 Attenuation of peak WT magnitudes for microcrack initiation source for various combinations of mode, frequency, source depth, and radiation angle.

For the  $A_0$  mode ratios for 60 kHz (Fig. 8), the in-plane dipole source is readily distinguished from the other two source types by any ratio of WT magnitudes in which at least one of the angles in the ratio is  $45^\circ$  or greater (e.g., WT magnitude for  $45^\circ$  / WT magnitude for  $0^\circ$ ). None of the  $A_0$  at 60 kHz ratios is particularly effective in distinguishing the microcrack from the shear source, although it can be noted that the microcrack ratio is always slightly less than the shear ratio for  $A_0$  at 60 kHz.

The  $S_0$  mode for 522 kHz (Fig. 9), readily distinguishes the shear source from the other two source types when at least one angle in the ratio is  $45^\circ$  or  $67.5^\circ$ . The ratio of the WT magnitude for  $67.5^\circ$  / WT magnitude for  $45^\circ$  has more moderate distinctions between the in-plane dipole and microcrack, yet also likely still maintains a reasonable peak WT magnitude.

Figures 10 and 11 display ratios for  $A_0$  at 270 kHz and  $S_0$  at 270 kHz, and one can see significant differences between the source types. These differences are similar in nature to those pointed out in figures 8 and 9. Upon closer examination of all 19 cases in the current database (i.e., three source types and six or seven source depths for each source type), the source type for eight of the 19 cases could be determined by using only primary WT angle ratios of the WT magnitude for  $45^\circ$  / the WT magnitude  $0^\circ$  at either  $A_0$  at 60 kHz or  $S_0$  at 522 kHz, as appropriate. But to uniquely identify the other 11 cases, it was additionally necessary to use secondary ratios from one of the following frequency-mode combinations:  $A_0$  at 270 kHz,  $S_0$  at 522 kHz,  $A_0$  at 270 kHz, or  $S_0$  at 270 kHz.

Successfully analyzing empirical AE data using the analysis approach described will obviously require giving greater consideration to various practical issues such as signal-to-noise ratios; however, the specific considerations necessary to account for noise issues are beyond the scope of this paper. In the present scenario (which used FEM AE signals without any noise), clearly the ability to uniquely identify the current set of three source types was possible using the angle-based ratio of WT magnitudes. Additional source types could likely also be identified using the same approach. For example, an out-of-plane dipole is an axisymmetric source, hence the angle ratios of WT magnitudes would all be equal to one.

## 6. Discussion of the Use of Normalized Single-Mode WT Magnitude Ratios for Various Radiation Angles for Source Identification

The technique described above does provide a means for the identification of the AE source type among the three source types considered. Due to symmetries in radiation patterns, the results from this study (which examined radiation angles from 0 to 90°) are directly applicable to radiation angles from 0 to 360°. The technique is successful because the radiation pattern of a particular mode and frequency is largely independent of the source depth over the range of depths for which the frequency-mode combination has a reasonable presence in the signal. However, developing the technique for use with experimental data will require additional research to resolve several issues.

The first issue to consider is the fact that when experimental data are recorded by multiple sensors located at various radiation angles from the source, it is highly unlikely that the propagation distances from the source to the various sensors will be equal. An approach to account for this scenario would be to use attenuation data such as those shown in Fig. 15 to correct the peak WT magnitudes at the different sensors to a common propagation distance. Straightforward research would need to confirm the success of such a basic approach.

A second issue regarding signal-to-noise (S/N) ratio is potentially more difficult to resolve. Electronic noise magnitudes in recorded AE signals are similar for all radiation angles and propagation distances. Thus, when one recalls that the peak WT magnitudes for AE signals do fall off (sometimes greatly) at larger radiation angles (see Figs. 12-14), it becomes apparent that the contributions of electronic noise may overwhelm the AE displacements for signals recorded at certain radiation angles from the source (perhaps 60 to 90°, and angles related to these by radiation symmetry). Thus, at larger radiation angles, the noise may be sufficiently great (compared to the AE signal) that the peak WT magnitude and/or its arrival time for the selected mode could be determined at best only inaccurately (or not at all). Such inaccuracy could result in the value of peak WT magnitude recorded as being greater or lesser than the actual value (caused by additive or negative reinforcement of the AE signal by the noise), or the arrival time of the WT peak may not correctly correspond to the mode of interest. Either type of error may give a peak WT magnitude not associated with or representative of the actual mode of the AE signal. Even for those events in which the signal magnitudes are quite large for the primary frequency, it is still desirable for the magnitudes from a secondary frequency also to be sufficiently large to be usable (for cases when the secondary frequency information is necessary to distinguish between source types), which may not be possible if the secondary S/N ratios are too low, as may occur even at moderate radiation angles.

The aspect of S/N ratios and their effect on the ability to perform source identification will be studied in detail in future research. Such a study can be done by use of a technique in which recorded electronic noise signals are numerically added in various amounts to finite-element-modeled AE signals; a study using a similar technique has already been completed, and has made a significant first step in examining the effect of S/N ratios on the accuracy of determined WT-based arrival times for calculating source locations [9].

Finally, it is not necessary to normalize the WT peak magnitudes by the 0° magnitudes, since direct ratios of WT peak magnitudes at two different angles yield the same numeric result as ratios of normalized WT values, assuming the propagation distance is the same for both WT peak magnitudes. The normalization was useful, however, to compare the WT peak magnitude results

at different depths as a function of the radiation angle (as shown in figures 2 to 7) prior to taking ratios at two different angles.

## 7. Conclusions

The following conclusions apply to the results for the 4.7 mm thick aluminum plate. For other materials and/or plate thicknesses, appropriate changes in key frequencies and associated modes will be necessary. These changes could likely be predicted using modeled AE signals.

A primary benefit of WTs versus other potential analysis techniques for AE signals is that magnitude information is created as a function of both time and frequency, thus allowing a focused examination at specific frequencies of particular interest and determination of arrival times of various modes. Wideband AE data is thus necessary to take advantage of the frequency information produced by the WT.

The exploration of energetic combinations of fundamental modes and frequencies of interest that are present in wideband AE data is made possible by the use of WT information in conjunction with group velocity curves.

The radiation pattern of the peak WT magnitudes (as normalized by the  $0^\circ$  value) for a fixed frequency and mode is almost totally independent of source depth. For particular frequencies and modes, this radiation pattern changes as a function of the AE source type.

For the three source types studied (in-plane dipole, microcrack initiation, and  $45^\circ$  shear without a moment) and the six or seven depths considered, the source type can be uniquely identified by certain simple single-mode ratios of peak WT magnitudes because of the differences in radiation patterns among different source types. Specifically, the ratios must be based on data for the same AE propagation distance at two selected radiation angles by the use of the primary frequency-mode combination, and in some cases supplemented by the inclusion of secondary frequency-mode information. The choice of radiation angles must be given some care to ensure both that the peak WT magnitudes are sufficiently large (they are greatest at angles in the range of  $0^\circ$  to  $60^\circ$ , and related symmetric angles) and that the differences in the source types ratios are maximized (which occurs at angles in the range of  $45^\circ$  to  $90^\circ$ , and related symmetric angles).

For the plate studied, the key frequency-mode combinations that are necessary for unique source identification are  $A_0$  at 60 kHz,  $S_0$  at 522 kHz,  $A_0$  at 270 kHz, and  $S_0$  at 270 kHz.

## Acknowledgements

This work was partially supported by NASA Langley Research Center. We also acknowledge the original development of the finite element code by John Gary (retired) of NIST, Boulder, Colorado. We wish to express our gratitude to Prof. M. Takemoto, who released the source code of the wavelet transform that his group had developed; this wavelet transform source code was utilized in the creation of the AGU-Vallen Wavelet software. We also thank Dr. Y. Mizutani and Mr. Jochen Vallen for making the AGU-Vallen Wavelet software into a highly usable form. The contributions of all the above people have significantly advanced the field of acoustic emission.

## References

1. M.A. Hamstad, A. O’Gallagher and J. Gary, “Examination of the Application of a Wavelet Transform to Acoustic Emission Signals: Part 1. Source Identification”, *J. of Acoustic Emission*, **20**, 2002, 39-61.
2. D.J. Buttle and C.B. Scruby, “Characterization of Fatigue of Aluminum Alloys by Acoustic Emission – Part I: Identification of Source Mechanism,” *J. of Acoustic Emission*, **9**, (4), 1990, 243-254.
3. D.J. Buttle and C.B. Scruby, “Characterization of Fatigue of Aluminum Alloys by Acoustic Emission – Part II: Discrimination Between Primary and Secondary Emissions,” *J. of Acoustic Emission*, **9**, (4), 1990, 255-269.
4. C.B. Scruby, “Quantitative Acoustic Emission Techniques,” *Research Techniques in Nondestructive Testing*, Chap. 4, Vol. 8, ed. R. S. Sharpe, Academic Press Inc., London, 1985, pp. 141-210.
5. M. Ohtsu, “Radiation Pattern of Acoustic Emission,” *Zairyo*, **32**, (356) (Japanese), 1983, 577-583.
6. Vallen-Systeme GmbH, Munich, Germany, <http://www.vallen.de/wavelet/index.html>, 2001, software version R2002.0703.
7. M.A. Hamstad, “An Illustrated Overview of the Use and Value of a Wavelet Transformation to Acoustic Emission Technology,” <http://www.vallen.de/zdownload/pdf/hamstad.pdf>.
8. M.A. Hamstad, K.S. Downs, and A.O’Gallagher, “Practical Aspects of Acoustic Emission Source Location by a Wavelet Transform”, *Journal of Acoustic Emission*, **21**, 2003, xxx.
9. M.A. Hamstad, A. O’Gallagher and J. Gary, “Examination of the Application of a Wavelet Transform to Acoustic Emission Signals: Part 2. Source Location”, *Journal of Acoustic Emission*, **20**, 2002, 62-81.